

7-11-2013

AM-FM Analysis of Structural and Functional Magnetic Resonance Images

Alvaro Emilio Ulloa Cerna

Follow this and additional works at: https://digitalrepository.unm.edu/ece_etds

Recommended Citation

Ulloa Cerna, Alvaro Emilio. "AM-FM Analysis of Structural and Functional Magnetic Resonance Images." (2013).
https://digitalrepository.unm.edu/ece_etds/255

This Thesis is brought to you for free and open access by the Engineering ETDs at UNM Digital Repository. It has been accepted for inclusion in Electrical and Computer Engineering ETDs by an authorized administrator of UNM Digital Repository. For more information, please contact disc@unm.edu.

Candidate

Department

This thesis is approved, and it is acceptable in quality and form for publication:

Approved by the Thesis Committee:

_____, Chairperson

AM-FM Analysis of Structural and Functional Magnetic Resonance Images

by

Alvaro Emilio Ulloa Cerna

Electrical Engineer, Pontificia Universidad Católica del Perú, 2010

THESIS

Submitted in Partial Fulfillment of the
Requirements for the Degree of

Master of Science
Electrical Engineering

The University of New Mexico

Albuquerque, New Mexico

May, 2013

©2013, Alvaro Emilio Ulloa Cerna

Dedication

To my wife and son, Jessica and Gabriel, for being the main motivation of my work.

To my parents, Emilio and Norma, for their unconditional support.

*To the memory of my grandmother Florencia for setting an example of dedication
and hard work for the family.*

*“Let your light shine before men, that they may see your good works, and glorify
your Father which is in heaven.” – Matthew 5:16*

Acknowledgments

I would like to thank my advisor Dr. Pattichis for his constant guide and advice in this thesis.

Moreover, I thank Dr. Rodriguez for his trust and encouragement to pursue a graduate degree.

Also, I would like to thank Dr. Liu and Dr. Calhoun for their collaboration with the data provided and discussions on interpretation of the results.

Also, thanks to the members of the Medical Image Analysis laboratory for their comments and interest in this project. Specially to my friend Rogers for his time spent in this topic.

Finally, I express all my gratitude to my wife, Jessica, for her continuous support and love.

AM-FM Analysis of Structural and Functional Magnetic Resonance Images

by

Alvaro Emilio Ulloa Cerna

Electrical Engineer, Pontificia Universidad Católica del Perú, 2010

M.S., Electrical Engineering, University of New Mexico, 2013

Abstract

This thesis proposes the application of multi-dimensional Amplitude-Modulation Frequency-Modulation (AM-FM) methods to magnetic resonance images (MRI). The basic goal is to provide a framework for exploring non-stationary characteristics of structural and functional MRI (sMRI and fMRI).

First, we provide a comparison framework for the most popular AM-FM methods using different filterbank configurations that includes Gabor, Equiripple and multi-scale directional designs. We compare the performance and robustness to Gaussian noise using synthetic FM image examples. We show that the multi-dimensional quasi-local method (QLM) with an equiripple filterbank gave the best results in terms of instantaneous frequency (IF) estimation.

We then apply the best performing AM-FM method to sMRI to compute the 3D IF features. We use a t-test on the IF magnitude for each voxel to find evidence of significant differences between healthy controls and patients diagnosed with schizophrenia (n=353) can be found in the IF.

We also propose the use of the instantaneous phase (IP) as a new feature for analyzing fMRI images. Using principal component analysis and independent component analysis on the instantaneous phase from fMRI, we built spatial maps and identified brain regions that are biologically coherent with the task performed by the subject. This thesis provides the first application of AM-FM models to fMRI and sMRI.

Contents

List of Figures	xi
1 Introduction	1
1.1 Functional Magnetic Resonance Imaging	2
1.1.1 fMRI preprocessing	3
1.2 AM-FM demodulation methods	4
1.2.1 Channel Component Analysis, Dominant Component Analysis, and Multiscale AM-FM Analysis	5
1.2.2 Quasi-local n-dimensional demodulation	9
1.3 Motivation for Current Work	10
1.4 Thesis statement	10
1.5 Contributions	11
1.6 Thesis Overview	11
2 Detection of brain activity in fMRI time-series	12

Contents

2.1	Introduction	12
2.2	Linear Regression Analysis	13
2.3	Independent Component Analysis	15
2.4	4-D AM-FM demodulation	17
2.4.1	Generalized quasi-local one-dimensional demodulation	18
2.4.2	Methods comparison	20
3	Preliminary results from AM-FM analysis of functional and structural MRI	25
3.1	Brain masking	25
3.2	Preliminary data analysis	26
3.2.1	AM-FM Feature space	28
3.2.2	Time-frequency Analysis on Resting fMRI	28
3.2.3	Instantaneous frequency analysis of sMRI	29
4	Results	33
4.1	Task-related fMRI analysis	34
4.2	Resting-state fMRI analysis	36
4.3	Structural MRI analysis	37
5	Conclusion and future work	39
5.1	Conclusion	39

Contents

5.2 Future work	40
A Proof that $\omega(x) \in [0, \frac{\pi}{3}]$ when $R \in [-\infty, -1]$	41
B Proof that $\omega(x) \in [\frac{2\pi}{3}, \pi]$ when $R \in [1, \infty]$	43
References	45

List of Figures

1.1	AM-FM demodulation based on Dominant Component Analysis (DCA) and the Quasi-Eigenfunction Approximation (QEA). The input is the extended analytic signal denoted by $I(\xi)$. The QEA is applied in correcting the instantaneous amplitude. This correction can be error-prone since it depends on the estimate of the IF.	8
2.1	T -map that indicates the voxels that are active for which the coefficients for the (a) left visual field task, and (b) the right visual field task. The fMRI images depicts active pixels using low image intensity. Thus, darker pixels signify activation.	15
2.2	ICA components coherent with visuo-motor cortical regions and time courses for both tasks that the patient perform.	17
2.3	$\theta(R)$ and $\theta(-R)$ in the respective domain R	20
2.4	Frequency Discrimination Algorithm (FDA) block diagram. Where <i>demod. 1</i> represents eq. (1.3), <i>demod. 2</i> represents eq. (1.5), h_{LP} and h_{HP} are the low pass and the high pass filter respectively. . . .	21

List of Figures

2.5	AM-FM analysis filter-banks. (a) Directional Filter Bank (DFB), each band indexed from 0 to 7; (b) Block diagram of (c) Nonsub-sampled directional multiscale and multiresolution filterbank block diagram. [1] and (d) the Pyramidal Directional Filter Bank (PDFB) with a multiresolution and multiscale decomposition into octave bands and a directional decomposition by the DFB to each high-pass band increasing the number of bands with the scale. Adapted from [2].	22
2.6	(a) I_{chirp} with frequencies $\omega_{1,2} \in [0, \pi]$ (see eq. (2.3)) and (b) I_{cubic} with $x_0 = -6$ and $x_1 = 6$ (see eq. (2.4))	22
2.7	A single line of pixels showing the instantaneous frequency magnitude estimate for (a) QLM, and (b) QEA on I_{chirp} with gaussian noise.	24
2.8	Normalized error comparisons for different filter-banks. (a) Filter-bank comparison using QEA demodulation method, and (b) filter-bank comparison using generalized QLM demodulation method. Error bars denote the minimum and maximum error for 50 repetitions at the given noise level.	24
3.1	(a) Histogram of the fMRI data, (b) slice 14 of the mask and (c) masked fMRI.	26
3.2	Matrix plot of AM-FM features and BOLD fMRI for raw data (upper plot) and after edge and eye blinking artifacts have been removed (lower plot).	31

List of Figures

3.3	(a) Manually selected Principal component showing coherence with brain function using the feature space containing AM-FM functions and (b) coefficients of the component corresponding to IP and expected response (HRF) of the BOLD signal for the task exciting the right visual and motor cortices.	32
3.4	(a) Scatter plot of IF_S and IF_t and (b) bivariate histogram for one healthy subject. A logarithm transformation was applied for the probability frequencies in each bin to enhance visualization.	32
4.1	Instantaneous phase of axial slice 11 (left) and slice 24 (right) to show activation at visual and motor areas in the brain for a subject (a) in rest, (b) exciting left side and (c) right side of the brain.	34
4.2	(a) Histogram of the instantaneous phase and (b) Histogram of the raw fMRI data.	35
4.3	Biologically relevant ICA on instantaneous phase components for (a) left task and (b) right task.	36
4.4	(a) P-value map for each bin tested and (b) bins that passed Bonferroni correction.	37
4.5	$\log_{10}(p)$ thresholded at 5 with a T1 image as template.	38

Chapter 1

Introduction

Non-stationary image processing methods provide a powerful alternative to stationary approaches. Non-stationary analysis can provide significant new insight into the basic signal characteristics. In this Master's thesis, we explore non-stationarity exhibited in functional magnetic resonance imaging (fMRI) and structural magnetic resonance imaging (sMRI). It is known that MRI signals [3] and noise [4, 5] exhibit strong non-stationary characteristics.

For one-dimensional signals, the short-time Fourier transform (STFT) is a standard tool for exploring non-stationary characteristics. More generally, one-dimensional time-frequency analysis requires the use of the Wigner distribution and its derivatives [6]. One-dimensional Wavelet transforms provide a specific time-frequency analysis method [7, 6].

The Teager-Kaiser operator in [8, 9] provided an alternative method for studying one-dimensional non-stationary signals based on the use of amplitude modulated and frequency modulated (AM-FM) functions. This was further extended to two-dimensional AM-FM representations for digital images in [10] and [11]. Moreover, multi-dimensional FM modeling for non-stationary image structure was studied in

[12]. Recently, Dr. Murray introduced the use of multi-scale AM-FM decompositions in [13].

This introductory chapter is organized as follows. In sec. 1.1, we provide an general description of acquisition and pre-processing of fMRI data. In sec. 1.2, we provide an introduction to some of the basics of AM-FM models and AM-FM demodulation.

1.1 Functional Magnetic Resonance Imaging

fMRI is a non-invasive technique that provides an image of brain function through time [14]. This imaging technique gives information on blood oxygenation indirectly related to neuronal activity. The blood oxygen level dependent (BOLD) contrast changes through time as a series of three dimensional images collected while the subject may be receiving stimulus, performing a task or resting.

The MRI scanner induces a magnetic field that causes the protons to align their spins. Then, by introducing a pulse of magnetic energy perpendicular to the main magnetic field in the form of a radio frequency pulse (specific to the hydrogen atom due to its high concentration in the human body), the spins absorb energy and become excited [15]. The time it takes for the protons to return to their equilibrium magnetization is an exponential decay process with time constant parameters called transverse relaxation time, T_2 , and longitudinal relaxation time, T_1 . Also, the parameter T_2^* is a time constant that characterizes the exponential decay of the signal, due to spin-spin interactions (related to T_2), magnetic field inhomogeneities (magnetic field induced by the MRI machine), and susceptibility effects (physical property of the brain). The rapid decay of the T_2^* signal provides for a faster MRI scanning.

The time sampling interval, T_R , is designed to be long enough so that gray matter

Chapter 1. Introduction

tissue can fully recover in between pulses. Depending on the tissue of interest, parameters can be tuned to enhance its contrast with surrounding tissue.

The MRI signal is acquired from two orthogonal detectors which are put in complex form [16], where BOLD contrast is measured. The BOLD signal depends on the magnetic properties of blood carrying oxygen to the neurons (oxygenated) and residual blood after neurons have used the oxygen (de-oxygenated). Thus, BOLD indirectly indicates neuronal activity.

1.1.1 fMRI preprocessing

Following scanning, the fMRI data is pre-processed to enhance data quality and allow for improved statistical power. The pre-processing steps are performed using SPM 8 software as described in [17]. The basic steps include:

Step 1. Slice Timing

The slices are collected at different times and require synchronization to avoid signal biases. Slice timing correction is performed using sinc function interpolation.

Step 2. Realignment

Head motion during scanning, even in the order of millimeters, can still cause significant artifacts. Motion correction is achieved realigning a time-series of images acquired from the same subject using a least squares approach and a 6 parameter (rigid body) spatial transformation. Also, the fat chemical that envelops the brain causes a shift in the resulting image and the susceptibility map is not homogenous due to the air canals near the brain such as the auditory and nasal canals. This correction is performed using an estimate of the susceptibility map and reconstruction from the phase of the acquired image.

Step 3. Spatial Normalization

Spatial normalization involves image registration to the brain atlas to allow for comparisons among different individuals.

Step 4. Smoothing

Spatial smoothing is applied for improving the signal-to-noise ratio (SNR) to allow for better activation detection. Smoothing does not have a high impact on frequency estimation because it is only reducing amplitude and not distorting frequency content.

1.2 AM-FM demodulation methods

AM-FM demodulation methods are in constant growth and several applications have been presented. The list of application includes fingerprint classification [18], image segmentation [19, 20, 21], and ultrasound video analysis [22, 23, 24, 25], among others.

The AM-FM representation for multi-dimensional signals provides an effective model of non-stationary content [12]. For the AM-FM representation, a multi-dimensional signal $I(\mathbf{x})$ is expressed as a sum of AM-FM components using:

$$I(\mathbf{x}) \simeq \sum_{m=1}^M a_m(\mathbf{x}) \cos(\varphi_m(\mathbf{x})) \quad (1.1)$$

where \mathbf{x} represents a vector of spatio-temporal coordinates, $I(\mathbf{x}) : \mathbb{R}^k \rightarrow \mathbb{R}$ maps the voxel values for each coordinate \mathbf{x} , M is the number of components, $a_n > 0$ denote the instantaneous amplitude (IA) components, and φ_n denote the instantaneous phase (IP) components. Slowly-varying (amplitude) characteristics are modeled using the IA components. Significant changes in non-stationary frequency content are modeled using the IP components.

Given the multidimensional signal $I(\mathbf{x})$, the computation of the AM-FM components involves the estimation of the instantaneous amplitude functions $a_n(\mathbf{x})$, the instantaneous phase functions $\varphi_n(\mathbf{x})$, and the instantaneous frequency (IF) function defined as the gradient of the instantaneous phase:

$$\begin{aligned}\omega_n(\mathbf{x}) &= \nabla\varphi(\mathbf{x}) \\ &= \left(\frac{\partial}{\partial x_1}\varphi_n(\mathbf{x}), \frac{\partial}{\partial x_2}\varphi_n(\mathbf{x}), \dots, \frac{\partial}{\partial x_k}\varphi_n(\mathbf{x}) \right).\end{aligned}$$

1.2.1 Channel Component Analysis, Dominant Component Analysis, and Multiscale AM-FM Analysis

In this section, we introduce the most popular methods for deriving AM-FM models. In order of complexity, the simplest method is based on *Channel Component Analysis* (CCA), followed by *Dominant Component Analysis* (DCA) [10], and *multi-scale AM-FM analysis* [13].

CCA consists of the decomposition of the input signal into M components coming from M channels. DCA constructs a single AM-FM component by using the channel output with the highest IA estimate. The Multi-scale analysis applies DCA to different frequency bands.

AM-FM models use AM-FM demodulation methods in order to estimate the AM-FM functions IA and IP. With the exception of the quasi-local method (QLM), all other methods require the computation of the *extended analytic signal*. For a single AM-FM component, the *extended analytic signal* attempts to estimate a complex exponential $a(\mathbf{x})\exp(j\varphi(\mathbf{x}))$ from the real-valued input AM-FM component of $a(\mathbf{x})\cos(\varphi(\mathbf{x}))$. In multiple-dimensions, the *extended analytic signal* representation is approximated using three steps:

Step 1. Take the multidimensional Fast Fourier Transform of the input signal $I(\cdot)$.

Chapter 1. Introduction

$$\mathbf{F}(\omega) = \text{FFTN}(I(\mathbf{x}))$$

Step 2. Remove half of the spectrum by setting the components to zero and doubling the remaining components:

$$\mathbf{G}(\omega) = \begin{cases} 0, & \text{if } \omega_1 < 0 \\ 2\mathbf{F}(\omega), & \text{otherwise.} \end{cases}$$

Step 3. Take the inverse FFT to estimate the complex signal approximation.

$$\hat{I}_{AS}(\mathbf{x}) = \text{IFFTN}(\mathbf{G}(\omega))$$

Note that no signal information is lost through the computation of the extended analytic signal due to conjugate symmetry of the multidimensional Fourier Transform ($\mathbf{F}(\omega) = \mathbf{F}^*(-\omega)$) in real-valued signals.

The extended analytic signal \hat{I}_{AS} is then processed through a filter-bank. This procedure is outlined in Fig. 1.1, where the impulse responses of the filter-bank are given by: h_1, h_2, \dots, h_N . In the basic *channel component analysis* approach, the outputs from each filter are used to estimate the AM-FM components. This approach is clearly best if non-stationary components can be localized to specific bands that is represented in the left figure of Fig. 1.1.

The assumption that the AM-FM components cannot be constrained to specific frequency bands leads to DCA. In DCA, each AM-FM component $a_n(\mathbf{x})$, $\varphi_n(\mathbf{x})$ and $\omega_n(\mathbf{x})$ are computed at each voxel as shown in the right figure of Fig. 1.1. Then, the goal of the filterbank is to provide a voxel-based separation of the different AM-FM components. AM-FM components are extracted from different filters at each voxel.

In DCA, the dominant AM-FM component is selected by the channel that gives the largest IA estimate. Due to the need to capture non-stationary behavior, the

Chapter 1. Introduction

dominant filter can vary from voxel to voxel. Formally, we have the dominant IA determined using:

$$a(\mathbf{x}) = \max_{n \in [1, M]} \{a_n(\mathbf{x})\},$$

and the index of the maximum channel

$$\kappa(\mathbf{x}) = \operatorname{argmax}_{n \in [1, M]} \{a_n(\mathbf{x})\}$$

is then used in determining the instantaneous phase and instantaneous frequency estimates using

$$\varphi(\mathbf{x}) = \varphi_{\kappa(\mathbf{x})}(\mathbf{x}), \quad \text{and}$$

$$\omega(\mathbf{x}) = \nabla \varphi_{\kappa(\mathbf{x})}(\mathbf{x}).$$

The instantaneous frequency based on the QEA is estimated by:

$$\begin{aligned} \hat{\omega}_1 &= \cos^{-1} \left[\frac{\hat{I}_{AS}(x_1 + 1, x_2, x_3, x_4) + \hat{I}_{AS}(x_1 - 1, x_2, x_3, x_4)}{2\hat{I}_{AS}(\mathbf{x})} \right] \\ \hat{\omega}_2 &= \cos^{-1} \left[\frac{\hat{I}_{AS}(x_1, x_2 + 1, x_3, x_4) + \hat{I}_{AS}(x_1, x_2 - 1, x_3, x_4)}{2\hat{I}_{AS}(\mathbf{x})} \right] \\ \hat{\omega}_3 &= \cos^{-1} \left[\frac{\hat{I}_{AS}(x_1, x_2, x_3 + 1, x_4) + \hat{I}_{AS}(x_1, x_2, x_3 - 1, x_4)}{2\hat{I}_{AS}(\mathbf{x})} \right] \\ \hat{\omega}_4 &= \cos^{-1} \left[\frac{\hat{I}_{AS}(x_1, x_2, x_3, x_4 + 1) + \hat{I}_{AS}(x_1, x_2, x_3, x_4 - 1)}{2\hat{I}_{AS}(\mathbf{x})} \right] \end{aligned}$$

An extension of DCA, called multi-scale analysis, was proposed by Dr. Murray in his dissertation [13]. In multi-scale analysis, we simply apply dominant component analysis over different collections of bandpass filters. The basic idea is to group together the different channel filters based on frequency magnitude. Thus, we can have low, medium, and high frequency scales. Furthermore, multi-scale analysis can take advantage of combinations of scales.

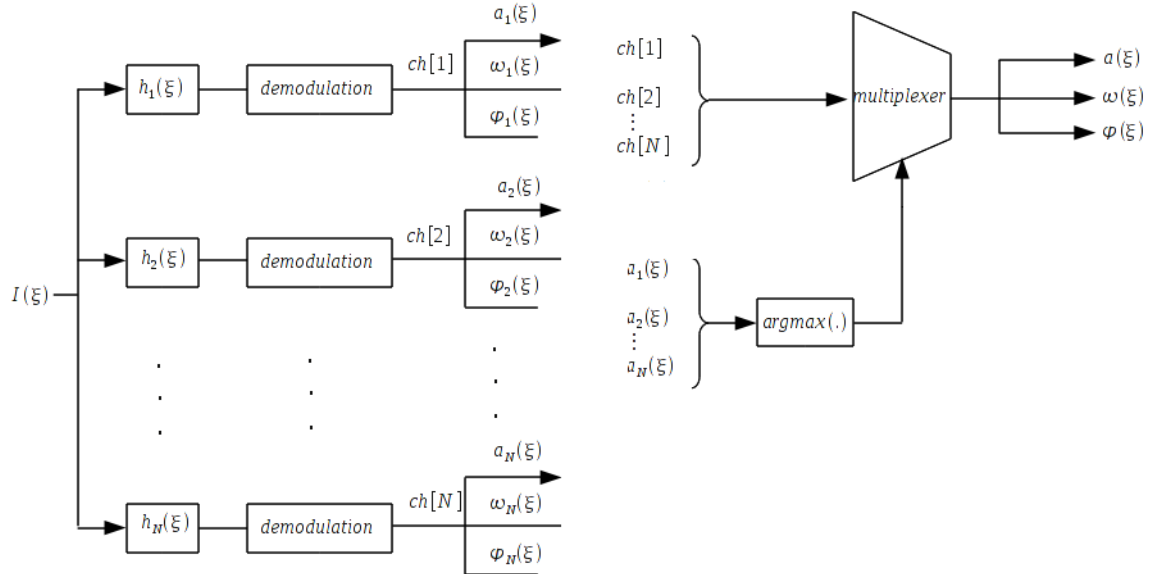


Figure 1.1: AM-FM demodulation based on Dominant Component Analysis (DCA) and the Quasi-Eigenfunction Approximation (QEA). The input is the extended analytic signal denoted by $I(\xi)$. The QEA is applied in correcting the instantaneous amplitude. This correction can be error-prone since it depends on the estimate of the IF.

The selection and design of an appropriate filter-bank can significantly affect the resulting AM-FM decomposition. Ideally, filterbank design should reflect the properties of the signals that are being analyzed. General-purpose Gabor-based filter-banks were used in Pattichis et al. [21] and Havlicek et al. [26]. Separable, flat-passband filters were used by Rodriguez in [24]. More recently, Dr. Murray [27] implemented a dyadic, separable and multiscale filter-bank using equiripple filters. Given the fact that the filter-bank can significantly impact the estimated AM-FM components, in Chapter 3, I compare accuracy between estimates derived using both Gabor and equiripple filter-bank designs.

1.2.2 Quasi-local n-dimensional demodulation

For the quasi-local method, estimation is based on products of samples of AM-FM components. We begin by defining

$$g_{(\epsilon_1, \epsilon_2)} = I(\mathbf{x} + \epsilon_1)I(\mathbf{x} - \epsilon_2),$$

where $(\epsilon_1, \epsilon_2 \geq 0)$, and $I(\mathbf{x}) = a(\mathbf{x}) \cos \varphi(\mathbf{x})$. Then, the instantaneous amplitude can be estimated using

$$a(\mathbf{x}) = \sqrt{2\check{g}_{(0,0)}(\mathbf{x})} \quad (1.2)$$

where $\check{g}_{(\epsilon_1, \epsilon_2)}(\mathbf{x}) = h_{LP}(\mathbf{x}) * g_{(\epsilon_1, \epsilon_2)}(\mathbf{x})$ and $h_{LP}(\mathbf{x})$ is a low pass filter. The low-pass filter is used for removing second-order, higher-frequency terms. For the purposes of this research, the low-pass filter was designed using an equiripple design with frequency cut-off set to $\pi/10$, a transition band of $\pi/10$, passband ripple at 0.017 dB, stop-band attenuation of 66.02 dB as described in [13, sec. 3.3].

Assuming that the instantaneous frequency satisfies $\omega(\mathbf{x}) < \pi/2$, it can then be estimated using

$$\omega(\mathbf{x}) = \cos^{-1} \left(\frac{R(\mathbf{x}) + \sqrt{R^2(\mathbf{x}) + 8}}{4} \right) \quad (1.3)$$

where

$$R(\mathbf{x}) = \frac{2\check{g}_{(1,1)}(\mathbf{x})}{\check{g}_{(1,0)}(\mathbf{x}) + \check{g}_{(0,1)}(\mathbf{x})}. \quad (1.4)$$

This operator is separable and applied to every dimension of the data. For $\pi/2 < \omega(\mathbf{x}) < \pi$, the instantaneous frequency is estimated as proposed in [24]

$$\omega(\mathbf{x}) = \pi - \cos^{-1} \left(\frac{-R(\mathbf{x}) + \sqrt{R^2(\mathbf{x}) + 8}}{4} \right) \quad (1.5)$$

1.3 Motivation for Current Work

Classical MRI analysis methods either assume stationarity or ignore non-stationary characteristics. The goal of this thesis is to apply AM-FM methods that are well-suited for analysing non-stationary signals to functional and structural MRI.

AM-FM methods provide a rich representation which allows the analysis in terms of the instantaneous amplitude, frequency, and phase for each voxel of the image. AM-FM functions can adapt to significant signal changes.

The thesis will explore the application of AM-FM methods to model brain dynamics and signal coherence in MRI images, providing a new data representation to compare between patients with mental diseases and healthy controls. The focus of the thesis is on the statistical analysis and interpretation of AM-FM components extracted from functional and structural MRI.

1.4 Thesis statement

The primary thesis of this dissertation is that the analysis of MRI data by AM-FM methods can lead to new insights into the non-stationary characteristics of structural and functional MRI.

First, we provide a comparison framework for the most popular AM-FM approaches to select an optimal method based on its performance in resistance to noise. Second, we apply the best-performing AM-FM demodulation method to functional and structural MRI where we explore its results with statistical tools. We compare sMRI instantaneous frequency in a case-control study using two independent sample t-test and logistic regression. Also, we use principal component analysis and independent component analysis on the instantaneous phase to describe its properties on

fMRI.

1.5 Contributions

The main contributions of the present work include:

- An AM-FM analysis framework for comparing demodulation methods (QEA and QLM) based on 3 filterbanks (Gabor, Equirple and Multiscale directional).
- A statistical analysis of MRI signals using a time-frequency non-stationary representation.
- An extended application of the instantaneous phase for detecting brain activity in functional images, and the use of the instantaneous frequency for representing brain structure.
- Provide evidence of significant differences between patients and healthy-controls given by AM-FM analysis that cannot be seen analyzing the raw data.

1.6 Thesis Overview

The thesis is organized into four parts. The first chapter presented a brief review of MRI data acquisition and AM-FM methods. The second chapter summarizes the classical methods used in brain activity detection and introduces the comparison framework. The third chapter describes the application of AM-FM methods to MRI and provides suggestions for differentiating between patients and healthy controls. Chapter four provides a discussion of the results. Finally, in the last chapter we provide our final conclusions based on the results and suggest future work.

Chapter 2

Detection of brain activity in fMRI time-series

2.1 Introduction

Despite the development of several approaches, the detection of true brain activity in fMRI scans remains an open problem. In this chapter, I summarize two of the most popular approaches.

The first approach is based on massive univariate statistical inference using a linear regression model. The BOLD signal is set as the response variable and task designed responses are set as the explanatory variables. These designed responses for each task are generated with the HRF convolved with a box-car (one for stimuli presence). Then, the model is fit for each voxel independently [28].

It is important to consider the multiple correction problem since we used a statistical test for determining whether each voxel is linearly related of the designed BOLD response or not. The probability of rejecting the null hypotheses $H_0 : \beta = 0$

when it is true (false rejection), increases with the number of tests. Thus, we may have a large probability of making one or more false rejections of the true H_0 . The most conservative way to correct the p-values is using Bonferroni p -value correction for voxels inside the brain only.

Multivariate approaches can help model brain connectivity represented by temporal correlations among spatially separated brain regions. A popular multivariate method for fMRI is based on Independent Component Analysis (ICA). ICA has been applied for the identification of various signal-types in the spatial or temporal domain, second level analysis of fMRI data and for the analysis of complex-valued fMRI data [29]. ICA can be applied without the need to have a-priori models for brain activity and produce spatially independent components (component images) or temporal independent components (component time courses).

In the remaining part of the Chapter, we introduce the use of the two most popular methods for brain analysis for fMRI data: linear regression analysis in Section 2.2 and independent component analysis (ICA) in Section 2.3. Also, we propose an adaptation of the AM-FM analysis methods for analysing MRI images is given in Section 2.4.

2.2 Linear Regression Analysis

Statistical Parametric Mapping (SPM) is a popular software tool to construct and assess spatial statistical processes and test hypotheses about functional imaging data. In SPM, we specify each voxel time series as the response variable and, in case of a block design, the convolution of the stimulus function of experiment with the HRF as predictor variable.

Then, the estimated coefficients for each voxel or so called β maps show regions of

Chapter 2. Detection of brain activity in fMRI time-series

the brain in which the model respond to the predictors. SPM also provides T -values resulting of hypothesis testing on β with the estimated standard deviation associated with this coefficient. This allows a visual inspections of regions of the brain linearly related to the stimuli and analysis with previous anatomic and functional knowledge of brain.

Example T -maps are shown in Fig. (2.1). In the example, we have the fMRI scan of 1 subject performing a visual and motor task [30]. The task consists of a flickering checker board presented to the subject as a visual stimuli. This is presented for 15 seconds to the right side and it is followed by 5 seconds of rest to the subject. Next, the same visual stimuli are presented to the left side of the visual field for 15 seconds and finally 20 seconds rest to repeat of the same pattern four times. For simplicity, we show the T -map using as explanatory variables the two designed BOLD response that relates to each side stimuli. The T -map indicates with black values the voxels for which the coefficients significantly different from zero. Notice that motor and visual cortex are those with the highest T statistic. Since this is a univariate method and each voxel is tested independently, we note sparse isolated regions on the T -map that are not related to the stimuli. The main issue with this method is that we require a prior model of brain behaviour and a model of the BOLD response which may vary by subject. Furthermore, this is a massive univariate approach which requires correction of the observed significance by the number of comparisons which is equal to the number of intro-cranial voxels ($\sim 30,000$).

On the other hand, as we shall discuss next, multivariate approaches such as PCA and ICA work on whole images and can identify spatio-temporal patterns over voxels without the need to specify priori information.

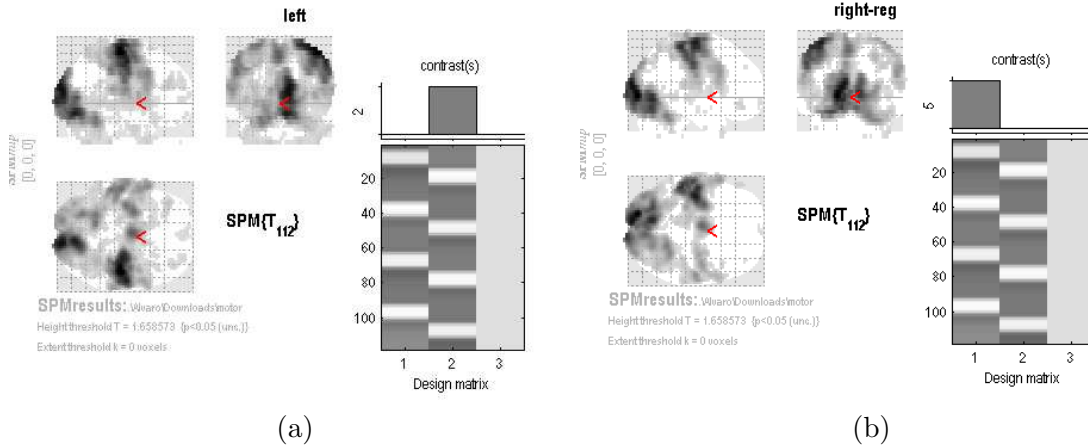


Figure 2.1: T -map that indicates the voxels that are active for which the coefficients for the (a) left visual field task, and (b) the right visual field task. The fMRI images depicts active pixels using low image intensity. Thus, darker pixels signify activation.

2.3 Independent Component Analysis

Independent component analysis is a multivariate method that separate a multivariate signal into additive components that are statistically independent. ICA seems to capture the essential structure of the data in many applications, including feature extraction and blind signal separation [31]. ICA find this components assuming that each observed signal is a linear mixture of n independent components.

In matrix form, we have $X = AS$ where X are the observed signals, A is the mixing matrix and S are the sources. Thus, the problem is to estimate A and S from X such that each source in S is as independent as possible. From $X = AS$, we have that each observation is represented as

$$x_j = a_{j1}s_1 + a_{j2}s_2 + \dots + a_{jn}s_n. \quad (2.1)$$

ICA cannot determine the variances of the independent components since any

scalar multiplier in A can be cancelled by a division in S . Also, the method can not determine the order of the independent components.

In addition, Gaussian sources are not separable in the ICA sense [32] because any orthogonal transformation will have the exact same joint distribution and thus we cannot estimate the mixing matrix A . To avoid this problem, we measure the kurtosis [33] and the neg-entropy [34] to determine whether an R.V. exhibits a normal distribution.

In order to estimate the sources, we first decorrelate the observation signals using a whitening matrix W . Higher order dependence can be partially addressed through rotations so as to minimize the dependence of the estimated sources. To minimize dependence, estimation proceeds by estimating A, W that minimize mutual information of the resulting source signals [35]. Similarly, A, W can be selected based on minimizing neg-entropy or maximizing the output entropy [36] (INFOMAX) among the sources. Alternatively, estimation can be performed using maximum likelihood estimation [37] among others.

ICA has become a very popular tool for fMRI analysis [29], mainly due to the consistency of its results with a priori biological knowledge regarding brain function. The assumption of ICA on fMRI is that activated regions of the brain do not overlap in time or space. Therefore, regions of the brain are independent sources that mix linearly and generate the observed fMRI data [38]. Also, it has been shown that fMRI noise is not Gaussian. In practice, most methods use the amplitude of the complex fMRI signal where the Gaussian noise of the real and imaginary part is transformed to Rician noise.

As an example, we apply ICA using the same data used in sec. 2.2 and show results using the software tool Group ICA Of fMRI Toolbox (GIFT) [39]. In this case, 15 independent sources were selected. In Fig. 2.2, we only show the two components

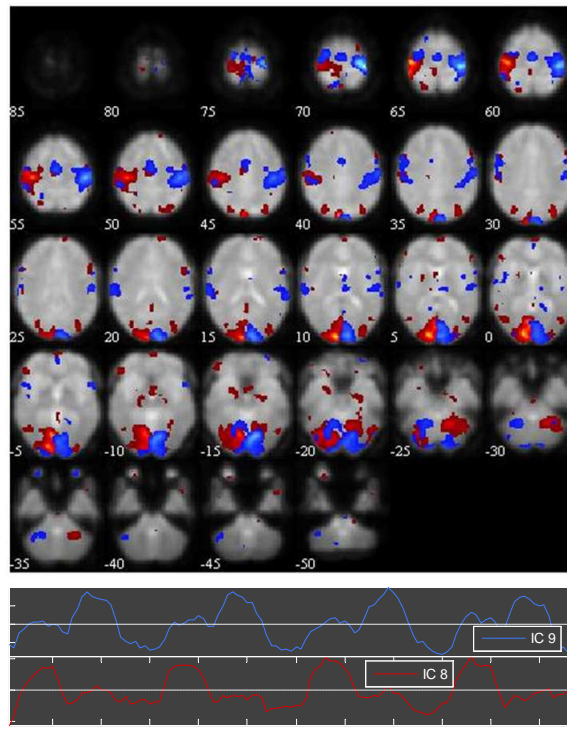


Figure 2.2: ICA components coherent with visuo-motor cortical regions and time courses for both tasks that the patient perform.

that are relevant to the task. We notice activation regions that extend beyond the visual and motor cortices. The results are consistent with the task and the Linear Regression results of Fig. 2.1.

2.4 4-D AM-FM demodulation

To the best of our knowledge, this is the first application of AM-FM methods to fMRI data. Furthermore, this is the first application of AM-FM models to 4D data sets. The application requires the design of a four dimensional filter-bank. In this application, we will consider the use of two AM-FM scales to avoid expensive computation.

The rest of this section is organized as follows. First, we provide details on the development of a new quasi-local method in section 2.4.1. Then, we evaluate performance on a synthetic example using three different filter-banks.

2.4.1 Generalized quasi-local one-dimensional demodulation

In this section, we propose a modification of the Quasi-local method to work with arbitrary frequency bands. The standard quasi-local method constrains the signal to either $[0, \frac{\pi}{2}]$ or $[\frac{\pi}{2}, \pi]$ and this constrains the design of the associated filter-bank. Therefore, we propose this new method in order to allow for generic filter-bank designs. Since the quasi-local approach is separable, we develop the one-dimensional algorithm that is applied along each dimension.

Let the monocomponent modulated signal be $f(x) = a(x) \cos \varphi(x)$, where $a(x)$ is the instantaneous amplitude and $\varphi(x)$ is the instantaneous phase. Also, let $\omega(x)$ be the instantaneous frequency of $f(x)$ computed with

$$\omega(\mathbf{x}) = \cos^{-1} \left(\frac{\pm R(\mathbf{x}) + \sqrt{R^2(\mathbf{x}) + 8}}{4} \right)$$

where

$$\begin{aligned} R(\mathbf{x}) &= \frac{2\check{g}_{(1,1)}(\mathbf{x})}{\check{g}_{(1,0)}(\mathbf{x}) + \check{g}_{(0,1)}(\mathbf{x})}, \\ g_{(\epsilon_1, \epsilon_2)} &= f(\mathbf{x} + \boldsymbol{\epsilon}_1)f(\mathbf{x} - \boldsymbol{\epsilon}_2), \end{aligned}$$

and $\boldsymbol{\epsilon}_1, \boldsymbol{\epsilon}_2 \geq 0$.

Then we know from sec. 1.2.2 that the problem is divided into two cases: $\omega(\mathbf{x}) < \pi/2$ and $\pi/2 < \omega(\mathbf{x}) < \pi$ for which we either apply eq. (1.3) or eq. (1.5) respectively.

We use a low-pass and high-pass filter to get two versions of $f(x)$ which are

$$\begin{aligned} f_1(x) &= h_{LP}(x) * f(x) \\ f_2(x) &= h_{HP}(x) * f(x) \end{aligned}$$

Chapter 2. Detection of brain activity in fMRI time-series

where h_{LP} has a passband of $0 < \omega < \pi/2$, and h_{HP} has a passband of $\pi/2 < \omega < \pi$.

Now, we define

$$\theta(R) = \frac{R + \sqrt{R^2 + 8}}{4} \quad (2.2)$$

where $\theta(R)$ is the argument of $\cos^{-1}(\cdot)$ in eq. (1.3) and $\theta(-R)$ becomes the argument of $\cos^{-1}(\cdot)$ in eq. (1.5).

Now, note that

$$0 < \cos^{-1}(\theta(R)) < \frac{\pi}{2}$$

, and

$$\frac{\pi}{2} < \pi - \cos^{-1}(\theta(-R)) < \pi$$

Then $R \in (-\infty, 1]$ and $-R \in [-1, +\infty)$.

Now, I plot the values of $\theta(R)$ and $\theta(-R)$ in Fig. 2.3, where we observe that $\theta(R)$ is monotonically increasing so $0 < \theta(R) < 0.5$ when $R \in (-\infty, -1]$. Using eq. (1.3) we can establish that $0 < \omega(x) < \frac{\pi}{3}$. Therefore, we use eq. (1.3) to estimate $\omega(x)$ (see proof in Appendix A).

Also, notice that $\theta(-R)$ is monotonically decreasing so $0 < \theta(-R) < 0.5$ when $R \in [1, \infty)$. Using eq. (1.5) we can establish that $\frac{2\pi}{3} < \omega(x) < \pi$. Therefore, we use eq. (1.5) to estimate $\omega(x)$ (see proof in Appendix B). Thus, we can choose what demodulation equation to use according to the computed value of R which is for $\omega(x) \in [0, \frac{\pi}{3}] \cup [\frac{2\pi}{3}, \pi]$. Finally, DCA is applied to select between $f_1(x)$ and $f_2(x)$ for $\omega(x) \in [\frac{\pi}{3}, \frac{2\pi}{3}]$ is computed and merged with the previous outcome. This process is outlined as a diagram block in Fig. 2.4.

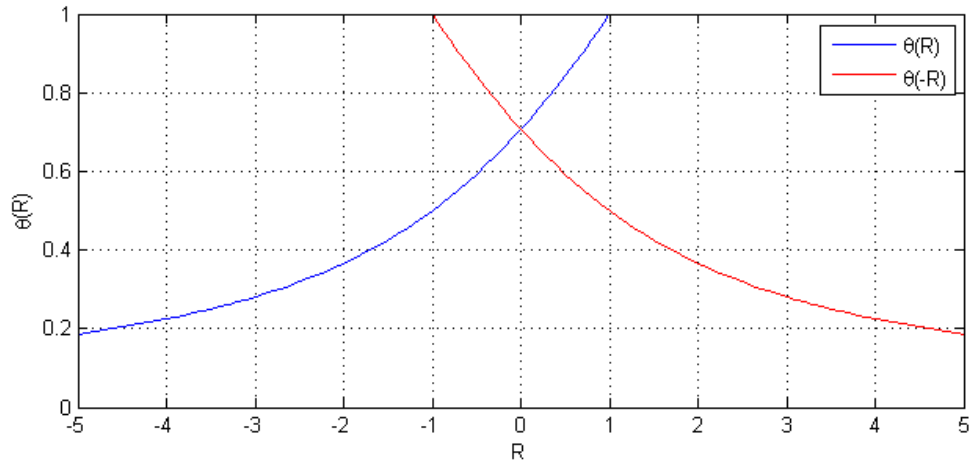


Figure 2.3: $\theta(R)$ and $\theta(-R)$ in the respective domain R .

2.4.2 Methods comparison

Filter banks

In order to have the most representative filter banks used for AM-FM demodulation we test three filter bank designs: (i) non separable Gabor filter bank [40, 10], (ii) separable filters designed by least squares optimization used in [24], (iii) and the directional multiscale and multiresolution filter bank of [1]. The Gabor filter bank is described in [10, sec. 4.4] and has been applied in [41, 42, 43]. The Gabor filter bank has also been used in models of the human visual system (e.g. see [10, sec. 2.2]). Separable filter banks designed based on least squares approximation in [24, sec. 3.2.8.1] provides for a direct approach. The directional multiscale and multiresolution filter-bank [2] provides an alternative approach.

In [2], the author states that a directional filter bank is made to support high frequency components (representing directionality) of images, so, low frequency components are handled poorly. Thus, in an effort to improve this problem, a multiresolution analysis is considered where low frequencies are partitioned with less directional

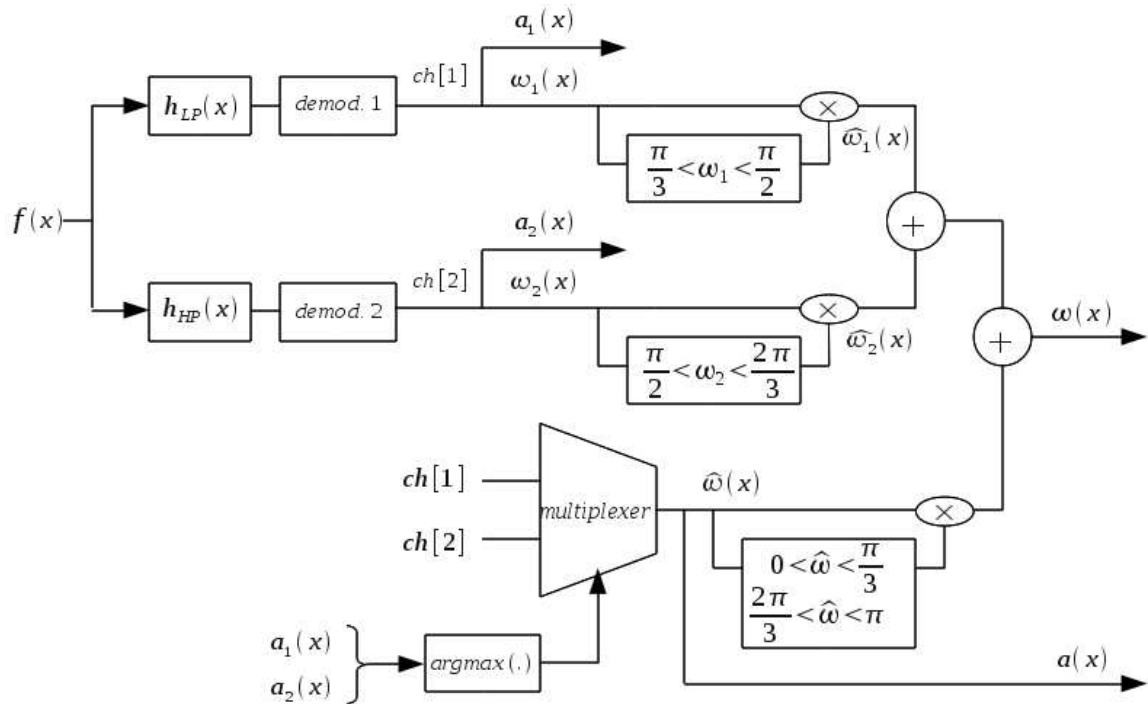


Figure 2.4: Frequency Discrimination Algorithm (FDA) block diagram. Where *demod. 1* represents eq. (1.3), *demod. 2* represents eq. (1.5), h_{LP} and h_{HP} are the low pass and the high pass filter respectively.

bands (see Figure 2.5d). The second approach is also used in the Nonsampled Contourlet Transform (NSCT) implemented in [1] which preserves the image size in each scale. According to [1], the NSCT results with better frequency selectivity and regularity when compared to the SCT.

Synthetic Frequency Modulation Images

We test the use of different filter-banks using two synthetic FM images. In particular, we test demodulation using quadratic and cubic phase examples.

The first synthetic example is based on a chirp image using:

$$I_{chirp}(x_1, x_2) = \cos \left[\frac{1}{2N}(ax_1^2 + bx_2^2) \right] \quad (2.3)$$

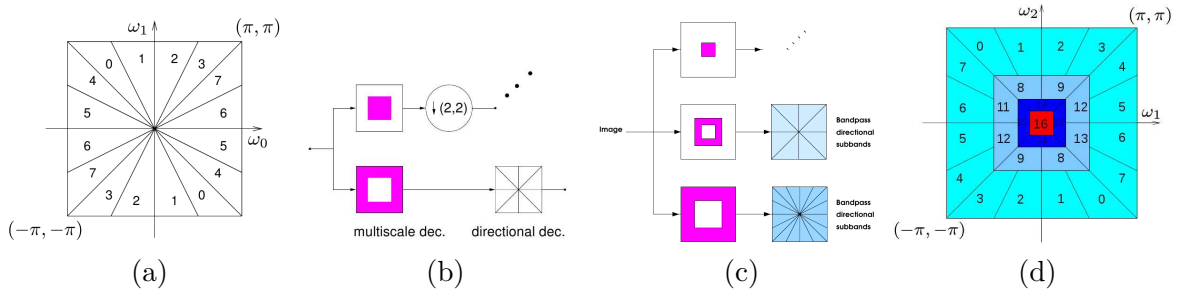


Figure 2.5: AM-FM analysis filter-banks. (a) Directional Filter Bank (DFB), each band indexed from 0 to 7; (b) Block diagram of (c) Nonsubsampled directional multiscale and multiresolution filterbank block diagram. [1] and (d) the Pyramidal Directional Filter Bank (PDFB) with a multiresolution and multiscale decomposition into octave bands and a directional decomposition by the DFB to each high-pass band increasing the number of bands with the scale. Adapted from [2].

where N is the number of pixels by side of the square image. The instantaneous frequency is set to vary from $-\pi$ to π in each direction. The resulting synthetic image is shown in Fig. 2.6a.

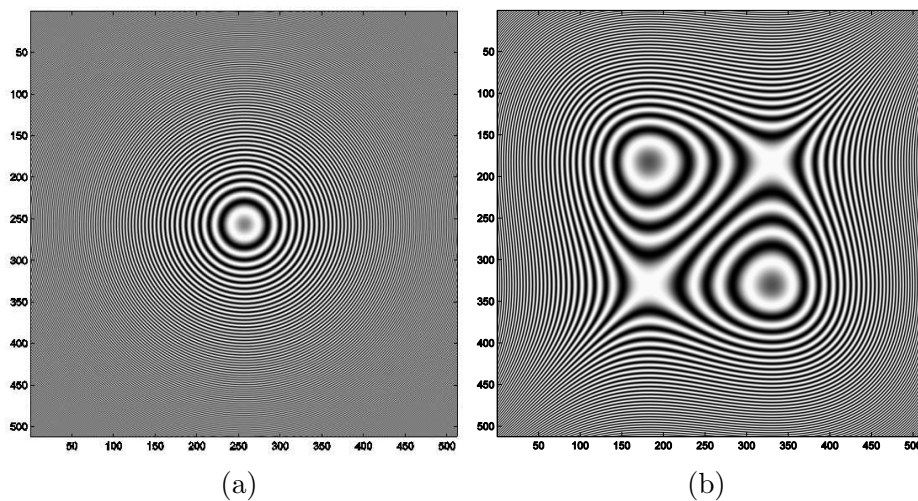


Figure 2.6: (a) I_{chirp} with frequencies $\omega_{1,2} \in [0, \pi]$ (see eq. (2.3)) and (b) I_{cubic} with $x_0 = -6$ and $x_1 = 6$ (see eq. (2.4))

The second synthetic example is generation using:

$$I_{cubic}(x_1, x_2) = \cos(x_1^3 + x_2^3 - ax_1 - bx_2) \quad (2.4)$$

where, the instantaneous phase is $\varphi(\mathbf{x}) = (x_1^3 + x_2^3 + 3ax_1 - 3bx_2)$, so the instantaneous frequency is:

$$\nabla\varphi(\mathbf{x}) = \omega(\mathbf{x}) = \left(\frac{\partial\varphi}{\partial x_1}, \frac{\partial\varphi}{\partial x_2}\right) = (3x_1^2 + 3a, 3x_2^2 - 3b).$$

We set $a = -6$ and $b = 6$ to achieve a maximum frequency to 0.3476 cycles/pixel as shown in the image in Fig. 2.6b. All images are of size 512×512 pixels.

Results

We measure the error in the instantaneous frequency using

$$error = \frac{\|\omega_t - \omega_{est}\|_2}{\|\omega_t\|_2} \quad (2.5)$$

where ω_t is the true value and ω_{est} is the estimated value. We use the term *normalized error* to refer to (2.5).

QLM estimation is not intended for use for very low or very high frequencies. We thus examine the error in the normalized frequency interval of $0.01\pi \leq |\omega| \leq 0.99\pi$. We also do not consider strong boundary artifacts by only measuring errors that are at-least 5 pixels away from the boundary of the image. In other words we do not consider the error in the upper, lower, left, and right edges of the image (see Fig. 2.7).

For final results in Fig. 2.8, we take the mean between the errors on I_{chirp} and I_{cubic} and report the error for each level of noise. The lowest error is given by the equiripple filterbank using the QLM demodulation method. This is the method that will be used for further analysis.

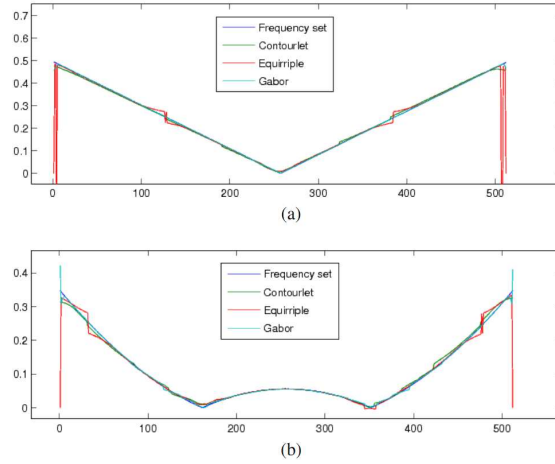


Figure 2.7: A single line of pixels showing the instantaneous frequency magnitude estimate for (a) QLM, and (b) QEA on I_{chirp} with gaussian noise.

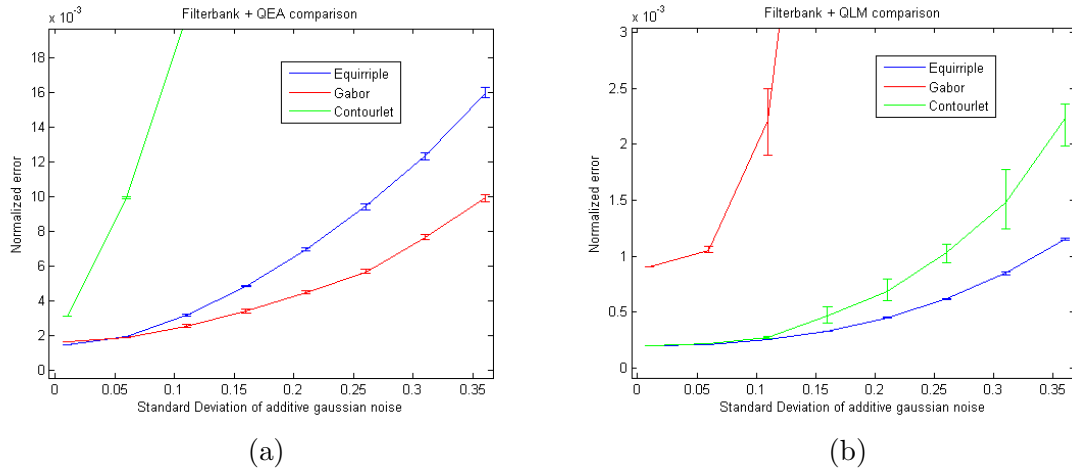


Figure 2.8: Normalized error comparisons for different filter-banks. (a) Filter-bank comparison using QEA demodulation method, and (b) filterbank comparison using generalized QLM demodulation method. Error bars denote the minimum and maximum error for 50 repetitions at the given noise level.

Chapter 3

Preliminary results from AM-FM analysis of functional and structural MRI

In this chapter, we explore AM-FM demodulation applied to sMRI and fMRI. The goal is to explore non-stationary behaviour in MRI using the extracted AM-FM features.

The outline of this chapter is as follows. In sec. 3.1, we describe the method for masking out data outside of the brain. In sec. 3.2, we explain our exploratory analysis and discuss preliminary results.

3.1 Brain masking

There are voxels that fall outside of the brain and are not of interest for the study. The boundary between intra-cranial voxels and background is fuzzy. In part, this is

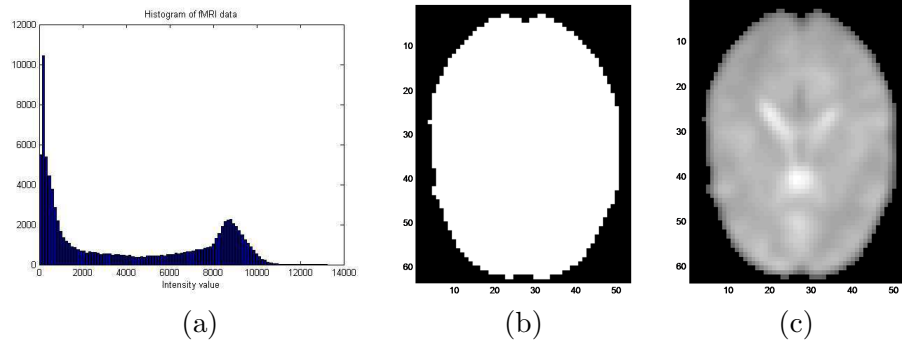


Figure 3.1: (a) Histogram of the fMRI data, (b) slice 14 of the mask and (c) masked fMRI.

due to the smoothing in the pre-processing steps. Therefore, we require a threshold to separate intra-cranial voxels from background.

A common method is to set the threshold to the mean value. The mean value is usually a valid threshold since around half of the total number of voxels are out of the brain. A more general approach for two dimensional images is proposed in [44]. It suggests to take the histogram of the image, smooth it and find the local minimum that discriminates the object from the background, assuming a bimodal distribution (see Fig 3.1). We extend this idea to the four dimensional data (fMRI). This approach provides a more general image segmentation for fMRI data not being dependent on the number of voxels covered by the brain in the four-dimensional data. In what follows, the analysis is applied only to voxels that are segmented as inside the cranium. See Fig. 3.1.

3.2 Preliminary data analysis

First, we focus on fMRI data collected from an experiment designed to stimulate visual and motor cortices, acquired with an echo planar sequence for a period of 3

minutes and 40 seconds, which gives a total of 220 time points with TR set to 1 second. See [30] for complete detail about acquisition and pre-processing.

The experiment is composed of three different task sequences. First, the subject is exposed only to a visual stimuli. Second, the subject performs to a motor task (finger tapping). Third, the subject is exposed to a visual stimuli while performs a motor task. We focus our study to the third sequence so the data set is reduced to 124 time points.

We compute IA, IF and IP estimations using QLM with an equiripple filter-bank designed with 17 coefficients, 2 scales, maximum amplitude ripple of 0.02 in the pass band, 0.2 maximum amplitude ripple in the rejection band and a 10% frequency spacing for the transitions. For filtering, we design a separable filter of $17 \times 17 \times 17 \times 17$ coefficients based on one 1D equiripple design as outlined earlier. The original dataset is of size $53 \times 63 \times 46 \times 124$. We discard the first 7 time points as in [30] and constrain the analysis to 117 time points where the subject performs a visual and motor task simultaneously.

For the exploration of the IF, IP and IA of the fMRI, we show a matrix plot that allows visual inspection of relationships between these AM-FM features and BOLD signals (see Fig. 3.2.a). From the plot, we notice that some values of the instantaneous frequency on time (IF_t) are well-separated from the primary distribution and appear to be outliers. A reconstruction of the location of these values in voxel space indicates that the outlying values are primarily due to eye blinking and, thus, not useful for our analysis. Blinking causes rapid changes in time and are not of interest.

In addition, the IP values close to $-\pi$ and $+\pi$ were found to be associated with the boundary between the brain and the background. Thus, these points were also removed. See Fig. 3.2.b for the data without blink eye effect and boundary effects.

3.2.1 AM-FM Feature space

In order to explore AM-FM features and their relation to brain function, first, we normalize the features to have zero mean and unit standard deviation across time. Then, we define a feature matrix composed by the concatenation of all AM-FM features along the time dimension, resulting in a matrix of 117×5 time points by the number of voxels. Each feature has 117 time points that are concatenated to form the feature space in the following order

$$[\hat{\omega}_1, \hat{\omega}_2, \hat{\omega}_3, \hat{\omega}_t, \hat{\varphi}_\xi].$$

Next, we reduce the number of time points using a Principal Component Analysis (PCA) to 92 features that keeps 95% of the total variance. Finally, we take the PCA components and display them as spatial maps. Visual inspection of each spatial map reveals that one of these components highlights the areas of the visual and motor cortices. Then, we examine the coefficients corresponding to this component and find evidence that the IP feature is related to the task (See Fig. 3.3). Notice that IP presents temporal coherence with the visuo-motor task given to the subject. This motivates further exploration of the IP and its relation to brain activity since, based on our observations, this is the most informative feature for task based fMRI.

3.2.2 Time-frequency Analysis on Resting fMRI

Resting-state fMRI is a functional scan of a resting subject and is usually performed to detect abnormal activity in patients using a functional connectivity model [45]. For instance, many studies on depression [46], autism [47], attention deficit hyperactivity disorder [48] and schizophrenia [49] (among others) have used resting-state fMRI.

Several approaches have been proposed for the analysis of resting fMRI [50, 51, 52] and a baseline study is proposed in [53], which, among other results, revealed strong

effects of age and gender in the power spectrum of certain regions in the brain. Moreover, frequency content has proven to be useful in the analysis of resting-state fMRI [54, 55]. However, a time-frequency analysis such as AM-FM demodulation has not been applied yet.

We therefore propose a scheme to process resting state fMRI with AM-FM functions as follows: First, we compute the AM-FM decomposition for each subject 4-dimensional data, from which we extract the instantaneous frequency over time (IF_t) and instantaneous frequency over space ($IF_s = \sqrt{IF_x^2 + IF_y^2 + IF_z^2}$); then, I create a bivariate histogram of IF_t and IF_s) with 20 bins for each feature and for each patient.

Each histogram summarizes the behavior of a subject in resting state. Thus, we would expect to find evidence of differences between patients and healthy controls by a comparison of these bivariate histograms. We proceed to compare each bin across groups to establish differences between patients and controls with a logistic regression. The regression model is built using a case or control indicator function as response and the bin proportion, age and gender as explanatory variables. Fig. 3.4 shows an example bivariate histogram for one healthy subject.

3.2.3 Instantaneous frequency analysis of sMRI

Structural MRI reveals brain anatomy (gray matter concentration) in higher spatial resolution than functional MRI. A natural approach is to extract texture information from gray matter concentration, which provides a description of the variation in intensity, including spatial patterns imperceptible to the naked eye. Texture analysis on MRI has proven successful for abnormality detection [56, 57]. Moreover, AM-FM decomposition have also proven useful for the study of lesions in multiple sclerosis patients [58].

Chapter 3. Preliminary results from AM-FM analysis of functional and structural MRI

The gray matter concentration value is subject to scanner variability either in multisite studies and even in the same scanner over time [59, 60]. On the other hand, the patterns of intensity variation are more likely to be consistent across different scanners with a consistent scanning protocol [61].

The strategy to compare between patients and healthy controls in the sMRI setting will be to obtain the IF_S for each voxel and use this information to test between groups using voxel-wise two sample t-tests with family-wise error correction.

Notice the for sMRI IF_t is not defined since no time information is available in this case.

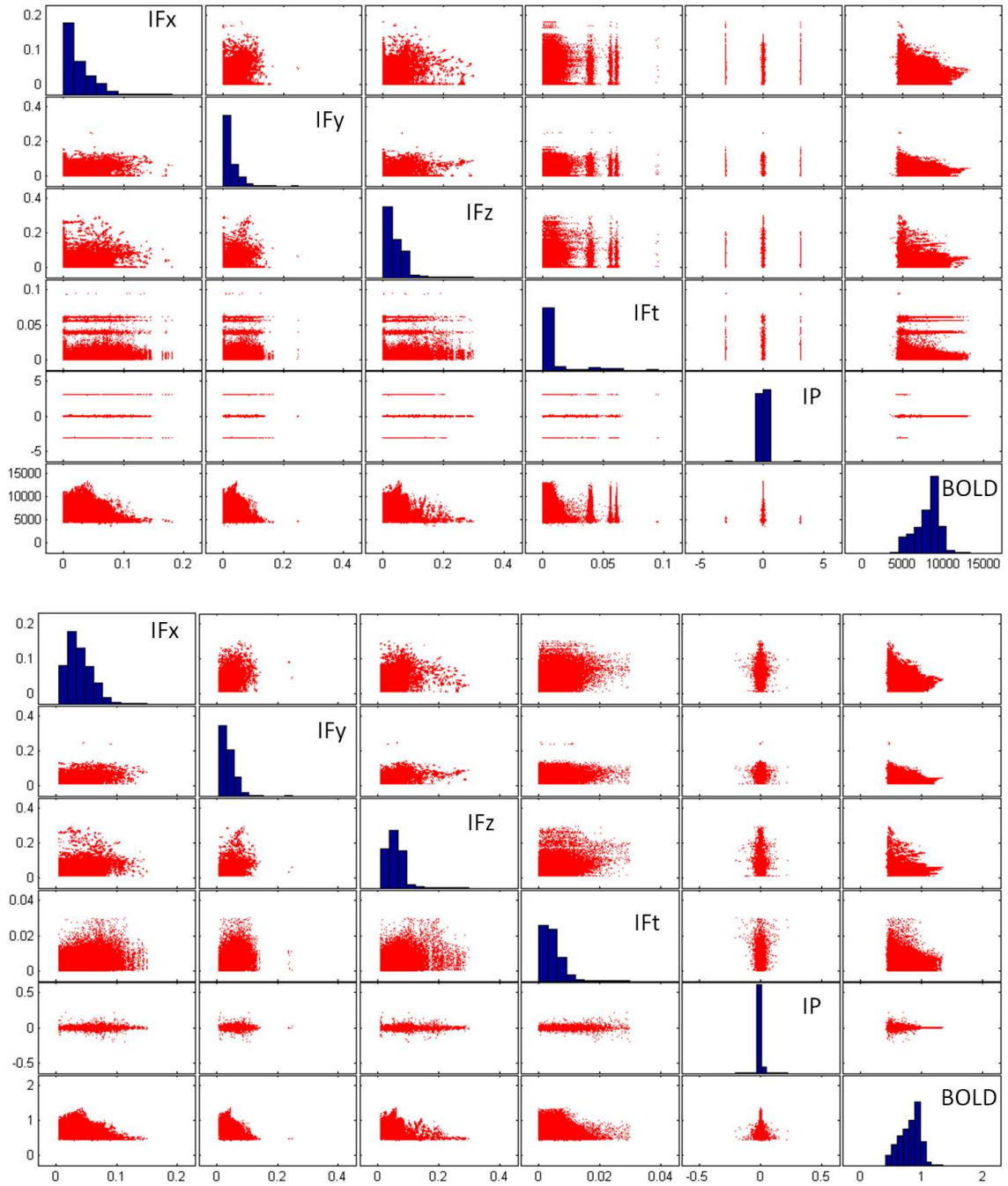


Figure 3.2: Matrix plot of AM-FM features and BOLD fMRI for raw data (upper plot) and after edge and eye blinking artifacts have been removed (lower plot).

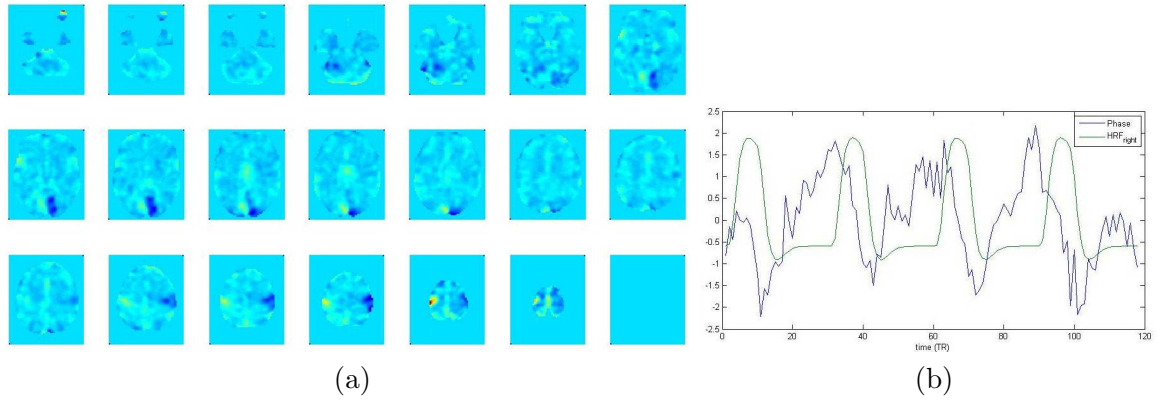


Figure 3.3: (a) Manually selected Principal component showing coherence with brain function using the feature space containing AM-FM functions and (b) coefficients of the component corresponding to IP and expected response (HRF) of the BOLD signal for the task exciting the right visual and motor cortices.

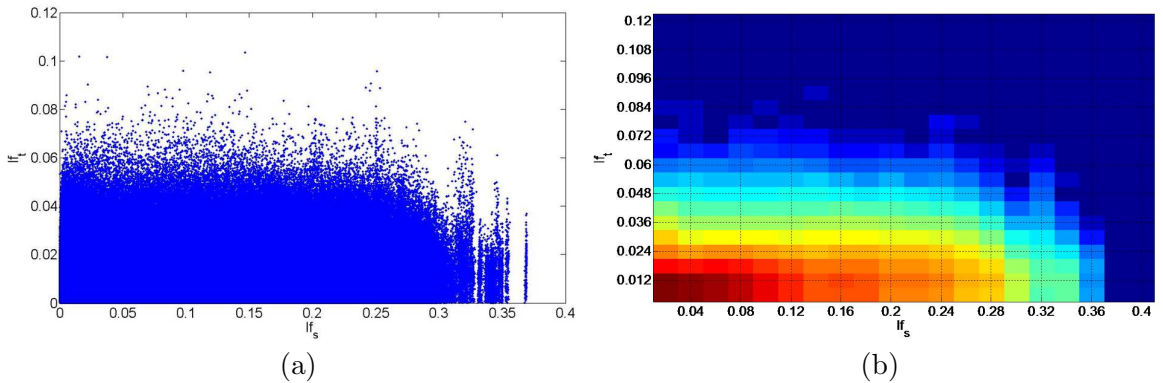


Figure 3.4: (a) Scatter plot of IF_S and IF_t and (b) bivariate histogram for one healthy subject. A logarithm transformation was applied for the probability frequencies in each bin to enhance visualization.

Chapter 4

Results

In the previous chapter, we suggested methods to analyze of AM-FM features of applied task-related fMRI, resting-state fMRI and structural MRI (sMRI). The goals were as follows:

Task fMRI: Identify brain regions that are biologically meaningful and whose temporal activity is in response to task stimulus.

Resting state fMRI: Use AM-FM features to detect abnormal activity in patients, as compared to healthy controls.

Structural MRI: Capture structural changes in gray-matter between patients and healthy controls.

In the present chapter, we show results of each method and discuss the advantages of applying this new form of data representation. First, we present the results of analyzing IP features from task-related fMRI. Then, we compare the bivariate histogram representations from resting-state fMRI of schizophrenia patients and healthy controls. Finally, we perform a mass univariate two sample test on the voxel-wise mod-

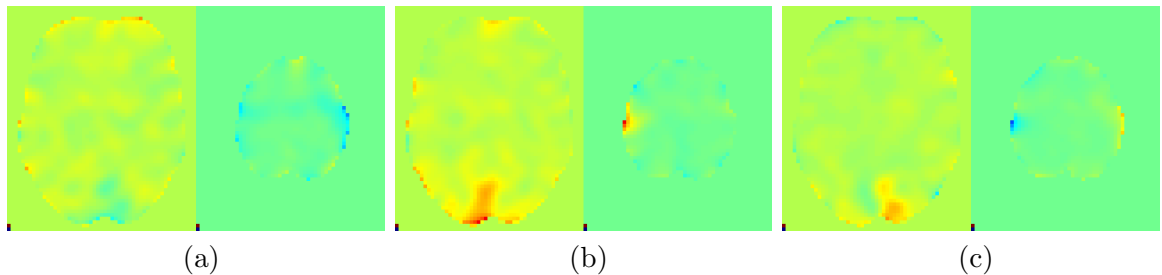


Figure 4.1: Instantaneous phase of axial slice 11 (left) and slice 24 (right) to show activation at visual and motor areas in the brain for a subject (a) in rest, (b) exciting left side and (c) right side of the brain.

ulo of the instantaneous frequency between patients with schizophrenia and healthy controls.

4.1 Task-related fMRI analysis

The patient performed a task that simultaneously excited visual and motor cortices in the brain. The scanning protocol of this subject is described in section 3.2. The data consist of a four dimensional hypercube of dimensions $53 \times 63 \times 46 \times 117$.

In section 3.2, we concluded that the IP is the most informative AM-FM feature. In the following, we further explore the properties of the instantaneous phase.

The IP responds to brain regions that are active, with a pattern in time that is coherent with the theoretical HRF-convolved stimulus. A visual inspection of the axial slices on the instantaneous phase in Fig. 4.1 shows it is sufficient to detect activation of visual and motor areas in the brain. Here, we note that this activation is not noticeable to the naked eye in the raw data.

The IP also reveals contrast in areas of the brain where we expect to show activity. The response in these areas is captured in form of de-phasing from the rest of the

Chapter 4. Results

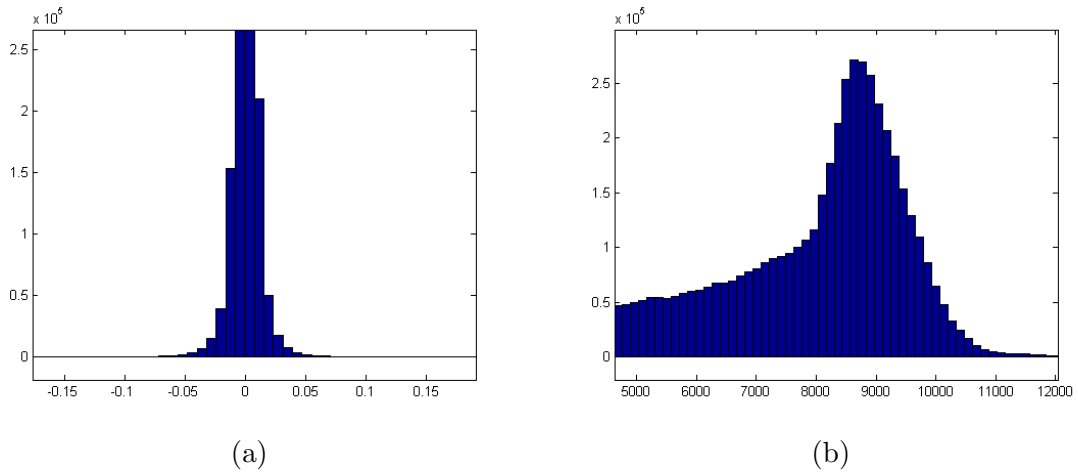


Figure 4.2: (a) Histogram of the instantaneous phase and (b) Histogram of the raw fMRI data.

brain. Therefore, we propose the use of the IP for detecting task-activated brain regions.

The distribution of the IP is highly kurtotic and has zero mean as shown in Fig. 4.2(a). This makes the IP adequate for a spatial ICA decomposition using the Infomax algorithm with sigmoid non-linearity and, thus, we explore independent IP components. In contrast, the distribution of the original data presents more Gaussian and sub-Gaussian features, like strong skewness and low kurtosis.

Next, we present the results of applying ICA to the IP feature (Fig. 4.3). Compared to the activation maps with better clustering obtained from the use of ICA on the original fMRI signal, ICA on IP provides maps of the visual and motor cortices, and, particularly, less granularity.

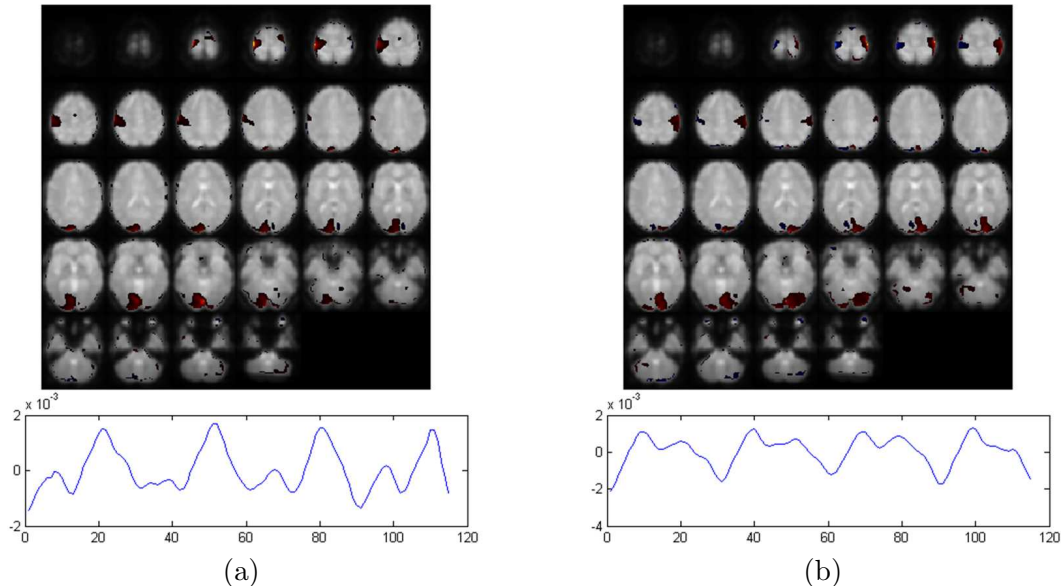


Figure 4.3: Biologically relevant ICA on instantaneous phase components for (a) left task and (b) right task.

4.2 Resting-state fMRI analysis

In this case, the data set consists of 369 subjects scanned while at rest. Among them, 180 have been diagnosed with schizophrenia while 189 were healthy controls. We compute the bivariate histogram of IF_s vs IF_t for each individual as previously described in sec. 3.2.2. This provides a unique representation for each subject.

Then, we fit a logistic regression model for each bin of the bivariate histogram using the following explanatory variables: the proportion value of the bin, age, gender and diagnosis as response variable. We also performed a backwards model selection procedure with the interactions. Then, we evaluated each model and dropped interaction terms that were not significant, i.e., with the significance level above 0.1. In Fig. 4.4, we show the bins for which coefficients were significant at the $p = 0.01$ level after Bonferroni correction ($0.01/400$). The figure shows evidence of differences

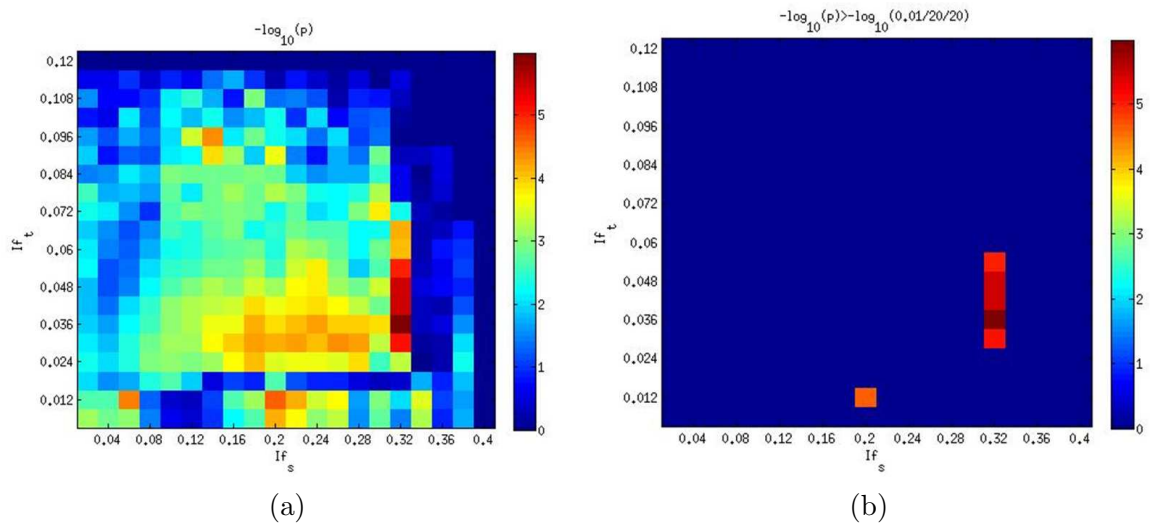


Figure 4.4: (a) P-value map for each bin tested and (b) bins that passed Bonferroni correction.

in certain, frequency bins, which we recommend as good features for automated diagnosis (classification) in the future.

4.3 Structural MRI analysis

Here, the data set consists on sMRI from 353 subjects. Among them, 165 are diagnosed with schizophrenia and 188 are healthy controls. In order to identify regions that are different between schizophrenic patients and healthy controls, we compare the IF magnitude at each voxel using a two sample t-test (significance level of 0.01 after Bonferroni correction).

From the results in Fig. 4.5, we can observe which voxels have higher mean IF magnitude in the patients, as compared to the healthy controls. This is evidence that the IF magnitude over a small brain region can be used to differentiate cases of schizophrenia from healthy controls (see Fig. 4.5).

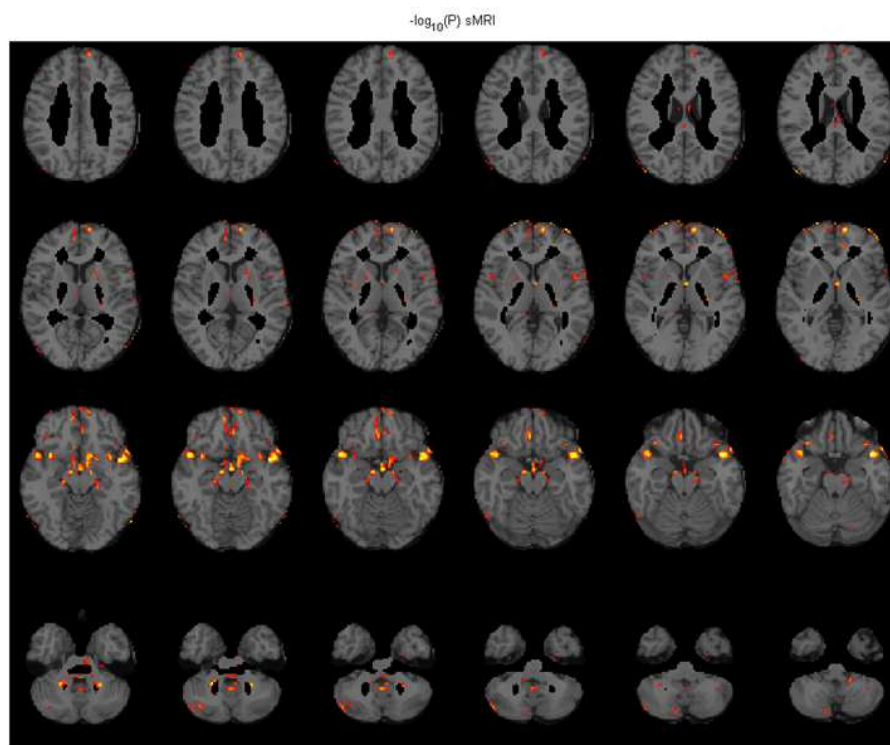


Figure 4.5: $\log_{10}(p)$ thresholded at 5 with a T1 image as template.

Chapter 5

Conclusion and future work

In this chapter, we provide final conclusions based on the results from the previous chapter and suggest future work.

5.1 Conclusion

In the thesis, the focus was to introduce the use of AM-FM analysis methods to MRI images. For analyzing MRI images, we first proposed a comparison framework for selecting the best combination of an AM-FM method and filterbank configuration. In terms of the mean square error of the IF magnitude estimation from a synthetic FM image. We found that the combination of the multi-dimensional quasi-local method with an equiripple filter-bank gave most accurate and robust to noise estimation.

The application of the quasi-local method with an equiripple filterbank gave the following results:

Structural MRI: The IF magnitude associated with gray matter concentration showed that select, local regions of the brain exhibited significant difference

between patients diagnosed with schizophrenia and healthy controls.

Resting fMRI: The joint-histogram of the IF spatial frequency magnitude ($||(\phi_x, \phi_y)||$) and the IF-time frequency component ($|\phi_t|$) provided for an effective characterization of brain activity. We fit logistic regression for each bin proportion value as a regressor along with age and gender showing evidence of abnormal proportions for one bin in schizophrenia patients.

Task fMRI: The instantaneous phase (IP) showed response to brain activity by identifying the regions that get out of phase compared to the rest of the brain.

AM-FM models has been applied in sMRI images for analysis of brain lesions in [58], although, to the best of our knowledge, this thesis is the first approach of AM-FM models to fMRI.

5.2 Future work

This section provides ideas for further research in this topic. Future work can address the following issues:

- Implementation of reconstruction from IP and IA on fMRI after ignoring IP values for low IA.
- Adaptive multi-scale AM-FM demodulation.
- Combination of ICA and IP can be studied as separation of multiplicative sources.
- Filterbank design for multicomponent analysis.
- Use of ICA for separating multiple components from a single channel.

Appendix A

Proof that $\omega(x) \in [0, \frac{\pi}{3}]$ when $R \in [-\infty, -1]$

Recall from sec. 1.2.2 that $\omega(x) = \cos^{-1} \theta(R)$ and $\theta(R) = \left[\frac{R + \sqrt{R^2 + 8}}{4} \right]$

First, notice that $\theta(R)$ is a monotonically increasing function.

Let $x_1 > x_2, \forall x_1, x_2 \in \mathbb{R}$

$$x_1 - x_2 > 0 \tag{A.1}$$

$$\sqrt{x_1^2 + 8} - \sqrt{x_2^2 + 8} > 0 \tag{A.2}$$

Now, adding eq. (A.1) and eq. (A.2)

$$\begin{aligned} x_1 + \sqrt{x_1^2 + 8} - x_2 - \sqrt{x_2^2 + 8} &> 0 \\ \theta(x_1) - \theta(x_2) &> 0 \end{aligned}$$

Appendix A. Proof that $\omega(x) \in [0, \frac{\pi}{3}]$ when $R \in [-\infty, -1]$

Then:

$$\begin{aligned} -\infty < R < -1 \\ \theta(-\infty) < \theta(R) < \theta(-1) \end{aligned}$$

where

$$\begin{aligned} \theta(-\infty) &= \lim_{R \rightarrow -\infty} \left[\frac{R + \sqrt{R^2 + 8}}{4} \right] \\ &= \lim_{R \rightarrow -\infty} \left[\frac{R + \sqrt{R^2 + 8}}{4} \right] \times \frac{(R - \sqrt{R^2 + 8})}{(R - \sqrt{R^2 + 8})} \\ &= \lim_{R \rightarrow -\infty} \frac{R^2 - (R^2 + 8)}{4(R - \sqrt{R^2 + 8})} \\ &= \lim_{R \rightarrow -\infty} \frac{2}{\sqrt{R^2 + 8} - R} \\ &= \frac{2}{\sqrt{(-\infty)^2 + 8} - (-\infty)} \\ &= \frac{2}{\infty} = 0 \\ \theta(-1) &= \frac{-1 + \sqrt{(-1)^2 + 8}}{4} \\ &= 0.5 \end{aligned}$$

Therefore: $0 < \theta(R) < 0.5$ and according to eq. (1.3) $0 < \omega(x) < \frac{\pi}{3}$.

Appendix B

**Proof that $\omega(x) \in [\frac{2\pi}{3}, \pi]$ when
 $R \in [1, \infty]$**

Recall from sec. 1.2.2, that $\omega(x) = \pi - \cos^{-1} \theta(R)$ and $\theta(R) = \left[\frac{-R + \sqrt{R^2 + 8}}{4} \right]$

First, notice that $\theta(R)$ is a monotonically decreasing function.

We have:

$$\begin{aligned} \frac{d\theta(R)}{dR} &< 0 \\ -\frac{1}{4} + \frac{R}{4\sqrt{R^2 + 8}} &< 0 \\ \frac{R}{\sqrt{R^2 + 8}} &< 1 \\ R &< \sqrt{R^2 + 8} \\ R^2 &< R^2 + 8 \\ 0 &< 8 \end{aligned}$$

Appendix B. Proof that $\omega(x) \in [\frac{2\pi}{3}, \pi]$ when $R \in [1, \infty]$

Then:

$$1 < R < \infty$$

and

$$\theta(1) > \theta(R) > \theta(\infty)$$

where

$$\begin{aligned} \theta(\infty) &= \lim_{R \rightarrow -\infty} \left[\frac{-R + \sqrt{R^2 + 8}}{4} \right] \\ &= \lim_{R \rightarrow -\infty} \left[\frac{-R + \sqrt{R^2 + 8}}{4} \right] \times \frac{(-R - \sqrt{R^2 + 8})}{(-R - \sqrt{R^2 + 8})} \\ &= \lim_{R \rightarrow -\infty} \frac{R^2 - (R^2 + 8)}{4(-R - \sqrt{R^2 + 8})} \\ &= \lim_{R \rightarrow -\infty} \frac{2}{\sqrt{R^2 + 8} + R} \\ &= \frac{2}{\sqrt{(\infty)^2 + 8} + (\infty)} \\ &= \frac{2}{\infty} = 0 \\ \theta(1) &= \frac{-1 + \sqrt{(1)^2 + 8}}{4} \\ &= 0.5 \end{aligned}$$

Therefore, $0 < \theta(R) < 0.5$ and according to eq. (1.5) $\frac{2\pi}{3} < \omega(x) < \pi$.

References

- [1] A. L. da Cunha, J. Zhou, and M. N. Do, “The nonsampled contourlet transform: theory, design, and applications,” *IEEE transactions on image processing: a publication of the IEEE Signal Processing Society*, vol. 15, pp. 3089–101, octubre 2006.
- [2] M. N. Do, *Directional multiresolution image representations*. PhD thesis, polytechnique Fédérale De Lausanne, E., 2001.
- [3] V. Calhoun, T. Adali, G. Pearlson, and J. Pekar, “Group ica of functional mri data: separability, stationarity, and inference,” in *Proc. Int. Conf. on ICA and BSS San Diego, CA. p*, vol. 155, 2001.
- [4] S. Kisner and T. Talavage, “Testing the distribution of nonstationary mri data,” in *Engineering in Medicine and Biology Society, 2004. IEMBS '04. 26th Annual International Conference of the IEEE*, vol. 1, pp. 1888 –1891, sept. 2004.
- [5] C. Long, E. Brown, C. Triantafyllou, I. Aharon, L. Wald, V. Solo, *et al.*, “Non-stationary noise estimation in functional mri,” *NeuroImage*, vol. 28, no. 4, p. 890, 2005.
- [6] L. Cohen, *Time-frequency analysis*, vol. 778. Prentice Hall PTR Englewood Cliffs, New Jersey, 1995.
- [7] I. Daubechies, “The wavelet transform, time-frequency localization and signal analysis,” *Information Theory, IEEE Transactions on*, vol. 36, pp. 961 –1005, sep 1990.
- [8] J. F. Kaiser, “On a simple algorithm to calculate the ‘energy’ of a signal,” in *Acoustics, Speech, and Signal Processing, 1990. ICASSP-90., 1990 International Conference on*, pp. 381 –384 vol.1, apr 1990.

References

- [9] J. F. Kaiser, “On Teager’s energy algorithm and its generalization to continuous signals,” in *Proceedings of IEEE DSP Workshop*, (New Paltz, NY), Sept. 1990.
- [10] J. Havlicek, *AM-FM image models*. PhD thesis, The University of Texas Austin, 1996.
- [11] M. Pattichis *et al.*, *AM-FM transforms with applications*. PhD thesis, The University of Texas at Austin, 1998.
- [12] M. Pattichis and A. Bovik, “Analyzing image structure by multidimensional frequency modulation,” *Pattern Analysis and Machine Intelligence, IEEE Transactions on*, vol. 29, pp. 753–766, may 2007.
- [13] V. Murray, *AM-FM methods for image and video processing*. PhD thesis, University of New Mexico, 2008.
- [14] K. Kwong, J. Belliveau, D. Chesler, I. Goldberg, R. Weisskoff, B. Poncelet, D. Kennedy, B. Hoppel, M. Cohen, and R. Turner, “Dynamic magnetic resonance imaging of human brain activity during primary sensory stimulation,” *Proc. Natl. Acad. Sci.*, vol. 89, pp. 5675–5679, 1992.
- [15] D. Noll, “A primer on mri and functional mri,” tech. rep., University of Michigan, Ann Arbor, USA, 2001.
- [16] D. I. Hoult, C.-N. Chen, and V. J. Sank, “Quadrature detection in the laboratory frame,” *Magnetic Resonance in Medicine*, vol. 1, no. 3, pp. 339–353, 1984.
- [17] Institute of Neurology, UCL, 12 Queen Square, London WC1N 3BG, UK, *SPM8 Manual*, February 2012.
- [18] M. S. Pattichis, G. Panayi, A. Bovik, and H. Shun-Pin, “Fingerprint classification using an am-fm model,” *IEEE Transactions on Image Processing*, vol. 10, pp. 951–954, 2001.
- [19] N. Ray, J. Havlicek, S. T. Acton, and M. S. Pattichis, “Active contour segmentation guided by am-fm dominant component analysis,” in *Proc. IEEE International Conference on Image Processing*, pp. 78–81, 2001.
- [20] T. B. Yap, J. P. Havlicek, and V. DeBrunner, “Bayesian segmentation of am-fm texture images,” in *Proc. 35th Asilomar Conf. Signals, Syst., Comput.*, vol. 2, pp. 1156–1160, 2001.
- [21] M. S. Pattichis, C. S. Pattichis, M. Avraam, A. Bovik, and K. Kyriakou, “Am-fm texture segmentation in electron microscopic muscle imaging,” *Acoustics, Speech, and Signal Processing*, vol. 4, pp. 2331–2334, 1999.

References

- [22] P. Rodriguez, M. S. Pattichis, and M. B. Goens, “M-mode echocardiography image and video segmentation based on am-fm demodulation techniques,” in *International Conference of the IEEE Engineering in Medicine and Biology Society*, 2003.
- [23] C. Christodoulou, C. Pattichis, V. Murray, M. Pattichis, and A. Nicolaides, “AM-FM Representations for the Characterization of Carotid Plaque Ultrasound Images,” in *4th European Conference of the International Federation for Medical and Biological Engineering*, pp. 459–546, Springer Berlin Heidelberg, 2008.
- [24] P. Rodriguez, *Fast and Accurate AM-FM demodulation of Digital Images With Applications*. PhD thesis, The University of New Mexico, 2005.
- [25] S. Murillo, M. Pattichis, C. Loizou, C. Pattichis, E. Kyriacou, A. Constantinides, and A. Nicolaides, “Atherosclerotic Plaque Motion Analysis from Ultrasound Videos,” in *Fortieth Asilomar Conference on Signals, Systems and Computers, 2006. ACSSC’06.*, pp. 836–840, 2006.
- [26] J. Havlicek and A. Bovik, *Image modulation models*, ch. 4, pp. 313–324. Burlington: Elsevier Academic Press, 2000.
- [27] V. Murray, P. Rodriguez, and M. Pattichis, “Multi-scale AM-FM Demodulation and Image Reconstruction Methods with Improved Accuracy,” *IEEE transactions on image processing*, 2010.
- [28] M. Martin, “Statistical analysis of fmri time-series: A critical review of the glm approach,” *Frontiers in Human Neuroscience*, vol. 5, no. 00028, 2011.
- [29] V. D. Calhoun, T. Adali, L. K. Hansen, J. Larsen, and J. J. Pekar, “Ica of functional mri data: An overview,” in *Proceedings of the International Workshop on Independent Component Analysis and Blind Signal Separation*, pp. 281–288, 2003.
- [30] V. D. Calhoun, T. Adali, and J. J. Pekar, “A method for comparing group fmri data using independent component analysis: application to visual, motor and visuomotor tasks,” *Magnetic Resonance Imaging*, vol. 22, pp. 1181–1191, 2004.
- [31] A. Hyvarinen and E. Oja, “Independent component analysis: algorithms and applications,” *Neural Networks*, vol. 13, pp. 411 – 430, 2000.
- [32] T. Lee, *Independent Component Analysis: Theory and Applications*. Springer, 1998.

References

- [33] K. V. Mardia, “Applications of some measures of multivariate skewness and kurtosis in testing normality and robustness studies,” *Sankhya: The Indian Journal of Statistics, Series B (1960-2002)*, vol. 36, no. 2, pp. pp. 115–128, 1974.
- [34] L. Brillouin, “The negentropy principle of information,” *Journal of Applied Physics*, vol. 24, pp. 1152 –1163, sep 1953.
- [35] A. Hyvarinen, “Independent component analysis by minimization of mutual information,” 1997.
- [36] A. Bell and T. Sejnowski, “An information-maximization approach to blind separation and blind deconvolution,” *Neural computation*, vol. 7, no. 6, pp. 1129–1159, 1995.
- [37] D. Pham and P. Garat, “Blind separation of mixture of independent sources through a maximum likelihood approach,” in *In Proc. EUSIPCO*, Citeseer, 1997.
- [38] V. Calhoun, T. Adali, G. Pearlson, and J. Pekar, “Spatial and temporal independent component analysis of functional mri data containing a pair of task-related waveforms,” *Human brain mapping*, vol. 13, no. 1, pp. 43–53, 2001.
- [39] N. C. Srinivas Rachakonda, Eric Egolf and V. Calhoun, *Group ICA Of fMRI Toolbox Manual*. The Mind Research Network, August 2004.
- [40] A. Bovik, “Variational pattern analysis using gabor wavelets,” in *ICASSP-92: 1992 IEEE International Conference on Acoustics, Speech, and Signal Processing*, 1992.
- [41] M. C. A. C. Bovik and W. S. Geisler, “Computational texture analysis using localized spatial filtering,” in *IEEE Computer Society Workshop Computer Vision*, 1987.
- [42] A. Bovik and M. Clark, “Multichannel texture analysis using localized spatial filters,” *Transactions on Pattern Analysis*, 1990.
- [43] M. Clark, “Texture discrimination using a model of visual cortex,” in *Proc. IEEE Conf. on Systems, Man and Cybernetics*, 1986.
- [44] J.-H. Chang, K.-C. Fan, and Y.-L. Chang, “Multi-modal gray-level histogram modeling and decomposition,” *Image and Vision Computing*, vol. 20, no. 3, pp. 203 – 216, 2002.

References

- [45] B. Biswal, F. Zerrin Yetkin, V. Haughton, and J. Hyde, “Functional connectivity in the motor cortex of resting human brain using echo-planar mri,” *Magnetic resonance in medicine*, vol. 34, no. 4, pp. 537–541, 1995.
- [46] M. Greicius, B. Flores, V. Menon, G. Glover, H. Solvason, H. Kenna, A. Reiss, and A. Schatzberg, “Resting-state functional connectivity in major depression: abnormally increased contributions from subgenual cingulate cortex and thalamus,” *Biological psychiatry*, vol. 62, no. 5, pp. 429–437, 2007.
- [47] D. Kennedy, E. Redcay, and E. Courchesne, “Failing to deactivate: resting functional abnormalities in autism,” *Proceedings of the National Academy of Sciences*, vol. 103, no. 21, pp. 8275–8280, 2006.
- [48] L. Tian, T. Jiang, Y. Wang, Y. Zang, Y. He, M. Liang, M. Sui, Q. Cao, S. Hu, M. Peng, *et al.*, “Altered resting-state functional connectivity patterns of anterior cingulate cortex in adolescents with attention deficit hyperactivity disorder,” *Neuroscience letters*, vol. 400, no. 1-2, pp. 39–43, 2006.
- [49] M. Liang, Y. Zhou, T. Jiang, Z. Liu, L. Tian, H. Liu, and Y. Hao, “Widespread functional disconnectivity in schizophrenia with resting-state functional magnetic resonance imaging,” *Neuroreport*, vol. 17, no. 2, pp. 209–213, 2006.
- [50] C. Beckmann, M. DeLuca, J. Devlin, and S. Smith, “Investigations into resting-state connectivity using independent component analysis,” *Philosophical Transactions of the Royal Society B: Biological Sciences*, vol. 360, no. 1457, pp. 1001–1013, 2005.
- [51] M. Greicius, B. Krasnow, A. Reiss, and V. Menon, “Functional connectivity in the resting brain: a network analysis of the default mode hypothesis,” *Proceedings of the National Academy of Sciences*, vol. 100, no. 1, pp. 253–258, 2003.
- [52] A. Di Martino, A. Scheres, D. Margulies, A. Kelly, L. Uddin, Z. Shehzad, B. Biswal, J. Walters, F. Castellanos, and M. Milham, “Functional connectivity of human striatum: a resting state fmri study,” *Cerebral cortex*, vol. 18, no. 12, pp. 2735–2747, 2008.
- [53] E. Allen, E. Erhardt, E. Damaraju, W. Gruner, J. Segall, R. Silva, M. Havlicek, S. Rachakonda, J. Fries, R. Kalyanam, *et al.*, “A baseline for the multivariate comparison of resting-state networks,” *Frontiers in systems neuroscience*, vol. 5, 2011.
- [54] D. Cordes, V. Haughton, K. Arfanakis, J. Carew, P. Turski, C. Moritz, M. Quigley, and M. Meyerand, “Frequencies contributing to functional connectivity in the cerebral cortex in resting-state data,” *American Journal of Neuroradiology*, vol. 22, no. 7, pp. 1326–1333, 2001.

References

- [55] P. Fransson, “Spontaneous low-frequency bold signal fluctuations: An fmri investigation of the resting-state default mode of brain function hypothesis,” *Human brain mapping*, vol. 26, no. 1, pp. 15–29, 2005.
- [56] J. Zhang, L. Tong, L. Wang, and N. Li, “Texture analysis of multiple sclerosis: a comparative study,” *Magnetic resonance imaging*, vol. 26, no. 8, pp. 1160–1166, 2008.
- [57] D. Mahmoud-Ghoneim, G. Toussaint, J. Constans, and J. de Certaines, “Three dimensional texture analysis in mri: a preliminary evaluation in gliomas,” *Magnetic resonance imaging*, vol. 21, no. 9, pp. 983–987, 2003.
- [58] C. Loizou, V. Murray, M. Pattichis, I. Seimenis, M. Pantziaris, and C. Pattichis, “Multiscale amplitude-modulation frequency-modulation (am–fm) texture analysis of multiple sclerosis in brain mri images,” *Information Technology in Biomedicine, IEEE Transactions on*, vol. 15, no. 1, pp. 119–129, 2011.
- [59] V. Gradin, V.-E. Gountouna, G. Waiter, T. S. Ahearn, D. Brennan, B. Condon, I. Marshall, D. J. McGonigle, A. D. Murray, H. Whalley, J. Cavanagh, D. Hadley, K. Lymer, A. McIntosh, T. W. Moorhead, D. Job, J. Wardlaw, S. M. Lawrie, and J. D. Steele, “Between- and within-scanner variability in the calibrain study n-back cognitive task,” *Psychiatry Research: Neuroimaging*, vol. 184, no. 2, pp. 86 – 95, 2010.
- [60] V.-E. Gountouna, D. E. Job, A. M. McIntosh, T. W. J. Moorhead, G. K. L. Lymer, H. C. Whalley, J. Hall, G. D. Waiter, D. Brennan, D. J. McGonigle, T. S. Ahearn, J. Cavanagh, B. Condon, D. M. Hadley, I. Marshall, A. D. Murray, J. D. Steele, J. M. Wardlaw, and S. M. Lawrie, “Functional magnetic resonance imaging (fmri) reproducibility and variance components across visits and scanning sites with a finger tapping task,” *NeuroImage*, vol. 49, no. 1, pp. 552 – 560, 2010.
- [61] G. Collewet, M. Strzelecki, and F. Mariette, “Influence of mri acquisition protocols and image intensity normalization methods on texture classification,” *Magnetic Resonance Imaging*, vol. 22, no. 1, pp. 81 – 91, 2004.